

Recurrent circuits as multi-path ensembles for modeling responses of early visual cortical neurons

Yimeng Zhang Harold Rockwell Ge Huang Stephen Tsou Yuanyuan Wei

Tai Sing Lee

Computer Science Department and Neuroscience Institute
Carnegie Mellon University
Pittsburgh, PA 15213
tai@cnbc.cmu.edu

Abstract

In this paper, we showed that adding within-layer recurrent connections to feed-forward neural network models could improve the performance of neural response prediction in early visual areas by up to 11 percent across different data sets and over tens of thousands of model configurations. To understand why recurrent models perform better, we propose that recurrent computation can be conceptualized as an ensemble of multiple feed-forward pathways of different lengths with shared parameters. By reformulating a recurrent model as a multi-path model and analyzing the recurrent model through its multi-path ensemble, we found that the recurrent model outperformed the corresponding feed-forward one due to the former’s compact and implicit multi-path ensemble that allows approximating the complex function underlying recurrent biological circuits with efficiency. In addition, we found that the performance differences among recurrent models were highly correlated with the differences in their multi-path ensembles in terms of path lengths and path diversity; a balance of paths of different lengths in the ensemble was necessary for the model to achieve the best performance. Our studies shed light on the computational rationales and advantages of recurrent circuits for neural modeling and machine learning tasks in general.

1 Introduction

Feed-forward deep neural networks have been shown to be effective models for predicting neural responses of early visual areas in the brain [1–6]. However, abundant recurrent connections exist within and between visual areas [7, 8]. In this paper we tried to investigate two questions. Experimentally, we wanted to know whether deep neural networks with recurrent circuits can provide a better model for predicting neural responses of early visual areas; theoretically, we wanted to understand why recurrent models perform better from a computational perspective, if the answer to the first question were positive. To answer the first question, we trained a multitude of feed-forward and recurrent models under tens of thousands of different configurations over hyperparameters and data sets; experimental results showed that recurrent models explained neural responses of early visual areas better than typical feed-forward models with matched hyperparameters and model sizes, especially when there was less training data. To answer the second question, we developed a novel method to reformulate recurrent computation as an ensemble of feed-forward paths. Our method is based on the hypothesis that the advantage of the recurrent model rests on the ensemble of multiple feed-forward paths embedded in the recurrent computation and such multitude of paths makes the recurrent model more flexible compared to a feed-forward model. By analyzing the recurrent model

through this multi-path ensemble reformulation, we found that it outperformed the feed-forward one due to its compact and implicit multi-path ensemble that allows approximating the complex function underlying recurrent biological circuits with efficiency. In addition, we found that the performance differences among the recurrent models we explored were highly correlated with the differences in their multi-path ensembles; in particular, models with more relative weights on shorter paths tended to perform better than models with more relative weights on longer paths. Our work establishes that the recurrent model outperformed the purely feed-forward model for predicting neural responses of early visual areas under tens of thousands of configurations, complementing previous studies on feed-forward models [1–3, 5] and consistent with very recent studies on recurrent ones [9, 10]. Our most interesting contribution is to establish that the superiority of the recurrent model for neural prediction can be attributed to the implicit and compact multi-path ensemble inside the model, and that a balance of different paths in the ensemble is necessary for the model to achieve the best performance. This work provides new understanding on the computational rationales and advantages of recurrent circuits that are ubiquitous in biological systems [7].

2 Related work

Modeling visual areas of the brain using neural network models with recurrent circuits In the brain, it is well known that there are local horizontal and long-range feedback recurrent connections [7, 11]. There are at least two types of studies involving recurrent circuits and deep neural networks. The first type focuses on showing the advantage of recurrent circuits in modeling temporal dynamics of visual neurons [10, 12–14]. Our work differs from them by demonstrating the superiority of recurrent models in the task of average firing rate prediction where feed-forward models are more likely to perform well than in the temporal case. Also, our work demonstrated the performance gain of recurrent models over feed-forward ones under tens of thousands of settings, whereas previous studies typically only trained and compared a couple of models. The second type uses recurrent circuits in the brain as a motivation and applies recurrent models to computer vision tasks such as image classification [9, 12, 13, 15]. Our work complements these by showing the advantage of recurrent models over feed-forward ones in neural modeling tasks [1, 2, 5] instead of computer vision ones.

Multi-path ensemble models and their relationships with recurrent models Multi-path models have been widely studied in the machine learning community; highway networks [16], ResNet [17, 18], FractalNet [19], and DenseNet [20] are among the most representative ones. Many multi-path models can be conceptually understood as ensembles summing over smaller networks [21]. Very few studies have connected recurrent models to multi-path ensemble models in the context of deep learning. There were some attempts to understand the relationship between recurrent models and deep networks. For ResNets, Liao and Poggio [22] did point out the equivalence between a specific type of recurrent networks with weight-tied ResNets, and Chen et al. [23] formulated deep weight-tied ResNets as approximating the dynamics of continuous recurrent models specified in ordinary differential equations. Bai et al. [24] found that weight-tied deep recurrent networks converge to a fixed point of the recurrent dynamics. Hinton and Salakhutdinov [25] pointed out that alternative Gibbs sampling in a restricted Boltzmann machine can be equated to an infinite logistic belief net with tied weights. To the best of our knowledge, there is no work explicitly connecting recurrent models to multi-path ensemble models in general. The most similar work to ours is likely Zhang et al. [26], which characterized recurrent models in terms of architectural complexity measures motivated by graph theory and quantified the relationship between performance and these complexity measures.

3 Methods

The modeling task is to predict the mean firing rate of each recorded neuron, given some input image. We approached this task by training and evaluating tens of thousands of feed-forward (Section 3.1) and corresponding recurrent models (Section 3.2) with matched model sizes and hyperparameters (Section 3.3). From an awake, behaving monkey, we collected neural responses of early visual areas (V1, V2) to two sets of static images, under two different stimulus presentation paradigms commonly used in the literature [5, 27]. In the **ImageNet 8K** data set, each stimulus was presented for a very short period (47 ms), and in the **NS 2250** data set, each stimulus was presented for a longer period (500 ms). The ImageNet 8K data set contains responses of 79 neurons to 8000 images from ImageNet

[28] with six trials collected per image per neuron; the NS 2250 data set contains responses of 34 neurons to the 2250 images used in Tang et al. [29] (CC BY 4.0) with 8 to 10 trials collected per image per neuron. More details can be found in Appendix A.

3.1 Baseline feed-forward models

Our baseline feed-forward models are based on those in Klindt et al. [2], Cadena et al. [5] (Fig. 1a) which are state of the art in predicting neural responses of early visual areas to our knowledge. We trained baseline feed-forward models of many different model sizes and hyperparameters (Section 3.3); each baseline model is a feed-forward model (Fig. 1a) that contains a batch normalization [30] layer, a set of convolutional processing blocks (CPBs), as well as pooling, fully connected, and activation layers. More details on the explored configurations (number of channels, type of activation function, etc.) can be found in Section 3.3, and a more detailed description of model inference can be found in Appendix B.1.

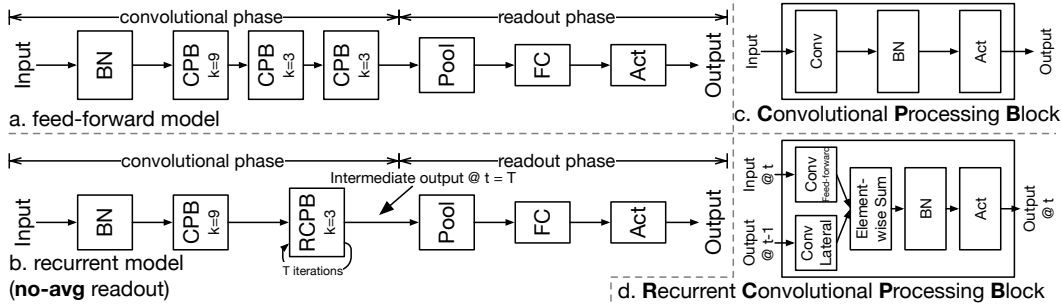


Figure 1: Models explored in this study. **(a)** shows an example baseline feed-forward model. **(b)** shows an example recurrent model under no-avg readout mode (Section 3.2). For both feed-forward and recurrent models, the model inference can be divided into two phases as shown at the top of **(a)** and **(b)**: convolutional and readout. The convolutional phase contains a BN layer followed by (recurrent) convolutional processing blocks, each of which contains convolution, BN, and activation layers; the readout phase takes the output of the final convolutional block through average pooling, factorized fully-connected [2], and activation layers to get the final model output. **(c)**, **(d)** show a convolutional processing block (CPB) and a recurrent convolutional processing block (RCPB), respectively. The kernel size of a (R)CPB is denoted by k in **(a)**, **(b)**. In this figure, we have in total three convolutional blocks for the feed-forward model **(a)** but only two blocks for the recurrent one **(b)** because a RCPB equals two CPBs in terms of model size; throughout this study we kept the first layer of a recurrent model to be feed-forward per pilot experiments (Appendix C.2).

3.2 Recurrent models

We explored the simplest possible recurrent variants [9] of our baseline feed-forward models. As shown in Fig. 1b, the general architecture of a recurrent model is similar to that of a baseline feed-forward model, with two differences which take place in the first phase (“convolutional phase” in Figs. 1a,b) and the second phase (“readout phase”) of the model inference process, respectively. A more detailed description of model inference can be found in Appendix B.2.

RCPB instead of CPB In the convolutional phase, a recurrent model replaces all but the first CPBs in a baseline feed-forward models with recurrent convolutional processing blocks (RCPBs). During model inference, information flows over each CPB only once whereas it flows over each RCPB for a certain number of iterations which is a model hyperparameter; when the number of model iterations is 1, a recurrent model is equivalent to a feed-forward one. A recurrent convolutional processing block (RCPB) extends regular CPB by having two inputs: a *bottom-up* input from the previous stage of the model in the current iteration and a *lateral* input from the output of the RCPB in the previous iteration (Fig. 1d). Note that while the convolutional layers (Conv Feed-forward and Conv Lateral) stay the same across different iterations during inference, the batch normalization layers are learned separately for each inference iteration, following Spoerer et al. [9]. Separately learning batch normalization layers makes the learning much easier and introduces negligible increase in model size (Section B.2, Appendix B.2).

Combination of intermediate outputs across iterations for the final output For a model with T iterations in total, the convolutional phase of model inference yields T intermediate outputs from the highest convolutional block, one for each iteration. While existing studies [15] mostly use the intermediate output at the last iteration to generate the final model output (Fig. 1b), in principle a recurrent model can also leverage intermediate outputs from earlier iterations to generate (read out) the final model output, explicitly taking account of dynamics and history in recurrent computation. There are multiple possibilities to combine intermediate outputs to generate the final predicted neural responses, and we explored four different ways, or readout modes (Fig. 2), which average intermediate outputs in different ways and differ in the number and location of averaging operations. Performance differences among recurrent models with different readout modes (Section 4.1) could be explained by the readout modes’ different weighting schemes on intermediate outputs (Sections 4.2,4.3).

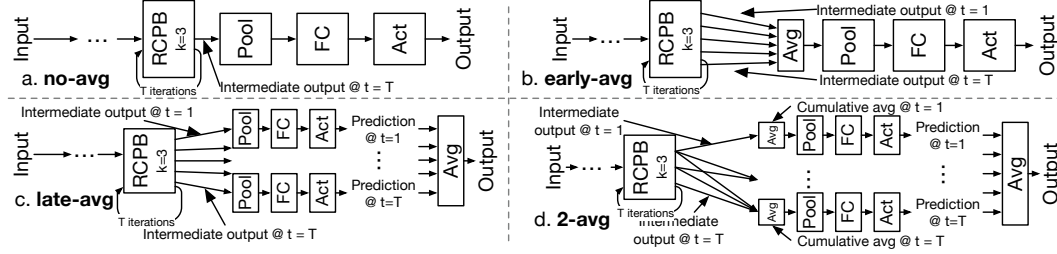


Figure 2: Readout modes no-avg (a), early-avg (b), late-avg (c), and 2-avg (d) explored in this study. The simplest one (no-avg) is also shown earlier in Fig. 1b. The style of the figure follows that of Fig. 1 and the convolutional phases which are the same across readout modes are omitted.

3.3 Implementation details

Model configurations We trained and tested tens of thousands of recurrent and feed-forward models under different configurations to comprehensively evaluate the performance gain of recurrent models over feed-forward ones. In total, for the ImageNet 8K data set, we trained 480 feed-forward models and 11 520 recurrent ones; for the NS 2250 data set, we trained 288 feed-forward models and 6912 recurrent ones. Under each data set, we trained a large number of feed-forward models with different amounts of training data (25 %, 50 %, 100 %), model sizes (by changing numbers of layers and channels), activation functions (ReLU or softplus), model initialization seeds, etc.; furthermore, to comprehensively compare feed-forward and recurrent models, for each feed-forward model, we trained 24 corresponding recurrent models of matched size and hyperparameters. These 24 recurrent models varied in two recurrence-related hyperparameters we explored: *number of iterations* (2 to 7), which affects the amount of recurrent computation of the model, and *readout mode* (no-avg, early-avg, late-avg, 2-avg; Section 3.2). More details can be found in Appendix C.2.

Model training For each data set, roughly 64 %, 16 %, and 20 % of images were allocated for training, validation, and testing, respectively. We constructed and trained all models using PyTorch [31] on the in-house computing cluster with 4-GPU (NVIDIA GeForce GTX 1080 Ti or similar) nodes. and followed Klindt et al. [2] on data preprocessing and model optimization details. See Appendices C.1, C.3 for details. Note that we trained models with different amounts of training data (Section 3.3)—25 %, 50 %, and 100 %—where the percentages are relative to the total available training data which constitute 64 % of the data as a whole.

Model performance evaluation Given a trained model, we use average CC_{norm}^2 [4, 32] over all neurons and all testing images (20 % of all images; Section 3.3) to quantify the model’s performance on a data set. Conceptually, CC_{norm}^2 measures the fraction of variance explained by the model, with trial-to-trial variance in neural responses discounted. To get the CC_{norm}^2 for a neuron, we first compute the raw Pearson correlation CC_{raw} between the ground truth trial-averaged neural responses and the model responses, then we divide CC_{raw} by CC_{max} , which estimates the maximal Pearson correlation coefficient an ideal model can achieve given the noise in the neural data [32, 33], followed by squaring. See Appendix C.4 for details.

4 Results

4.1 Recurrent models outperformed similarly-sized feed-forward models

Figs. 3a,b,c compare individual feed-forward models with recurrent ones, under different combinations of readout mode and number of iterations (Section C.2), on the NS 2250 data set. Recurrent models consistently outperformed feed-forward ones (Fig. 3b and most panels in Fig. 3a), except for a few cases, such as no-avg readout mode combined with a high number of iterations (Fig. 3c). As a summary of recurrent vs. feed-forward models, Figs. 3d,e,f show the average performance metrics for feed-forward models as well as for each of 24 different types of recurrent models, when the models were trained on 100%, 50%, and 25% of training data, respectively (Section 3.3). With appropriate choices of readout mode and number of iterations, recurrent models outperformed feed-forward ones on the NS 2250 data set by around 11 % with 25 % training data and by around 5 % with all the training data (Table 1). Similar results on recurrent vs. feed-forward models held on the ImageNet 8K data, and those results can be found in Appendix D.

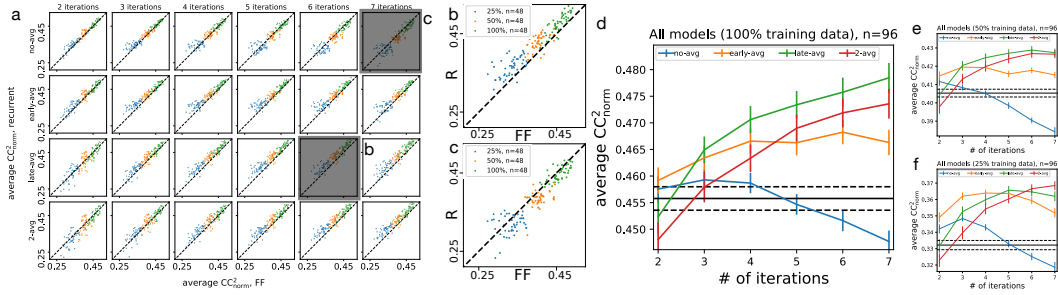


Figure 3: Recurrent models vs. similarly-sized feed-forward models on the NS 2250 data set. **(a)** shows recurrent models vs. feed-forward models under 24 combinations of readout mode and number of iterations over 24 panels, with rows for different readout modes and columns for different numbers of iterations; in each panel, models trained under different amounts of training data (25%, 50%, 100%) are shown in different colors, with 80 (aggregated) model pairs for each explored training data size. Each dot shows the performance of a recurrent model on the y axis vs. a feed-forward model of matched size and hyperparameters on the x axis; here model performance was calculated by averaging over multiple models with the same configuration on everything except for initialization seeds, to increase the robustness of metrics. **(b)** and **(c)** zoom into two particular panels in **(a)**. **(d)** summarizes all models trained on 100 % training data, with the horizontal solid line showing the average performance of feed-forward models trained on 100 % training data, and colored lines showing the average performance metrics of 24 types of recurrent models; dashed lines and error bars show s.e.m. **(e),(f)** are similar to **(d)** except that they summarize models trained on 50 % and 25 % of training data, respectively.

Table 1: Recurrent vs. feed-forward models on the NS 2250 data set. The three rows correspond to Figs. 3d,e,f, respectively. For each row, column 2 shows the average performance of feed-forward models (horizontal solid lines in the corresponding figure); column 3 shows the readout mode and number of iterations for the best recurrent model (highest colored data point) in terms of average performance; column 4 shows the relative performance gain of the recurrent model over the feed-forward one.

training data	FF avg perf	best readout mode, # of iter for R	performance gain (%)
25% (350)	0.3322	2-avg, 7	10.9439
50% (700)	0.4053	late-avg, 6	5.8053
100% (1400)	0.4558	late-avg, 7	4.9779

4.2 Approximation of recurrent blocks as multi-path ensembles

While recurrent models generally outperformed feed-forward ones (Section 4.1), we wanted to be able to explain these results. In particular, we wanted to answer two questions: 1) why did recurrent

models outperform feed-forward models? 2) why did recurrent models of different readout modes perform differently? To answer these questions, we reformulated each recurrent model as a multi-path model that is easier to analyze, inspired by Veit et al. [21]. In particular, the reformulation converts the recurrent model’s recurrent processing blocks (RCPBs) into an approximately equivalent multi-path ensemble with multiple feed-forward paths of different lengths. Fig. 4 illustrates the reformulation process. During model inference, recurrent blocks compute responses in an iterative fashion, resulting in multiple information flow paths of different lengths with shared components such as convolutional and batch normalization layers (Fig. 4a). To make the analysis of recurrent computation easier, we can approximate the actual information flow as summations of simpler feed-forward paths (Fig. 4b), separating shared components into separate individual paths. The resulting multi-path ensemble is a summation of multiple feed-forward paths with shared parameters.

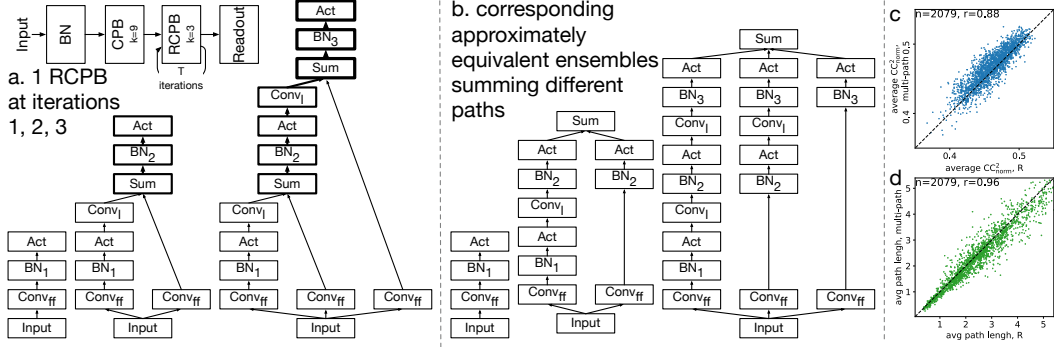


Figure 4: Recurrent computation approximately understood as summation of feed-forward chains of different lengths. (a) shows the information flows of a 1-layer RCPB at iterations 1, 2, and 3 during model inference; the width of a black line is proportional to the number of information flows passing between adjacent components and the width of a component’s border is proportional to the number of information flows passing through. (b) shows the information flows of corresponding multi-path ensembles and each flow sums over feed-forward chains of different depths. (c) compares multi-path models and original recurrent models in terms of model performance. (d) compares the two in terms of average path length of their multi-path ensembles. Models shown here were trained on all the training data. See Appendix E for details and additional results.

While the reformulation is approximate in nature, since it ignores the effects of activation functions and bias parameters in the derivation, in practice we found that the equivalence largely held, in the sense that the corresponding multi-path model trained from scratch and the original recurrent model were matched in multiple aspects. The reformulated and original models matched in their performance metrics (Fig. 4c) as well as some of their multi-path ensembles’ key characteristics such as average path length defined and used later in Section 4.3 (Fig. 4d). See Appendix E for details and additional results.

4.3 Understanding differences among models via average path length and path diversity

After establishing the approximate equivalence between recurrent models and multi-path models, we then treated each original recurrent model’s recurrent block(s) as a multi-path ensemble with the same parameters. Each multi-path ensemble has multiple paths of different lengths (Figs. 4b) and we found that differences among models could be mostly explained by two characteristics of the ensemble. The first one is *average path length*, weighted by the strength of each path; conceptually the average path length can be considered the *effective depth* of an ensemble. The second one is *path diversity*; models with similar average path lengths can be very different in terms of the contributions of individual paths; for example, an average path length of 3 can be either created from a single path of length 3 or five paths of lengths 1 through 5; intuitively, the latter model has higher diversity than the former; in this study, we use the path length distribution as a measure of diversity.

Fig. 5 demonstrates the computation of average path length and path diversity for an example recurrent model. The computation of length and diversity depends on the concept of *strength* for each component and each path. For a component on some path, roughly speaking, the strength of the component is a scalar measuring the ratio of the magnitude of the component’s output over that of its

input. In particular, we define the *strength* of each component as follows: the strength of a BN layer is the average of the absolute values of the scaling factors, over all output channels; the strength of a convolutional layer is the average of the 2-norms of the 3-D convolutional kernels flattened into vectors, over all output channels; the strength of an activation layer (ReLU or softplus in this study) is 1, as the activation layer outputs the input itself when the input is large enough. For a path, we define its strength to be the product of the strengths of all components along the path.

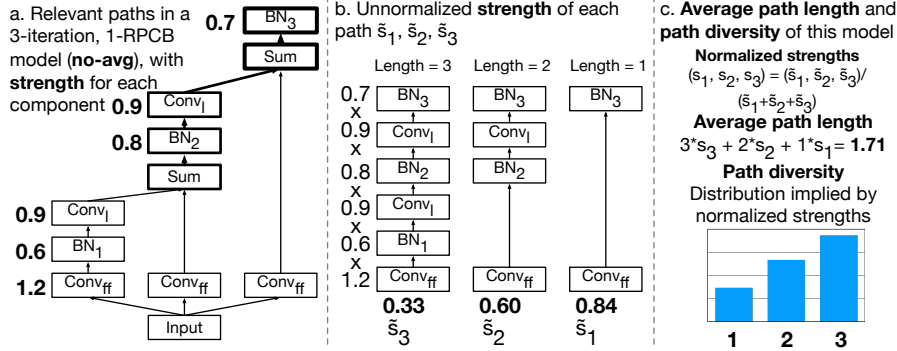


Figure 5: Computation of average path length and path diversity for an example recurrent model. The model has one recurrent block (RPCB) and uses the no-avg readout mode with three iterations. In (a), the relevant information flow is shown, with a *strength* assigned to each component. In (b), the original information flow is reformulated as a simple multi-path ensemble with three paths, and the unnormalized strength of each path $\tilde{s}_1, \tilde{s}_2, \tilde{s}_3$ is computed as the product of strengths along that path. In (c), the *average path length* of the model is defined as the average path length weighted by the normalized strengths s_1, s_2, s_3 , and the *path diversity* of the model is the discrete probability distribution implied by normalized strengths s_1, s_2, s_3 . The length of each path is defined as the number of convolutional layers in that path. Activation layers are omitted in (a) and (b) for brevity and they do not affect the calculation due to having a strength of 1.

4.3.1 Path length and diversity explained performance differences across readout modes

In Figs. 3d,6a,6b, performance vs. number of iteration curves for different readout modes were not well aligned, crossing each other at different vertical axis locations (especially Figs. 3d,6a), and no obvious connections and similarities among readout modes could be found from the curves. By reformulating recurrent models as multi-path models, (Section 4.2), we found that performance differences among readout modes and iterations were highly correlated with differences in the path length and diversity of the corresponding multi-path ensembles.

Average path length unified readout modes for shallow models As shown in Figs. 6c,d, curves of performance vs. average path length were much better aligned across different readout types, compared to Figs. 6a,b. In particular, when the average path length was relatively short (say, ≤ 2.5), all readout modes' curves were roughly the same; and when the path length was higher, curves began heading in different directions depending on the mode, due to differences in the path diversity explained below.

Balanced path distribution performed better with shorter paths playing more important roles While average path length could help unify different recurrent readout modes when the length was short, readout modes did behave differently as the length increased. In general, under similar average path lengths, late-avg/2-avg modes performed the best, early-avg performed slightly worse, and no-avg performed much worse (Figs. 6c,d).

We hypothesized that performance differences between readout modes were related to path diversity, when the average path length was similar. Figs. 6e,f show the path length distributions for different readout modes when their average path lengths were similar as denoted by black circles in Figs. 6c,d.

Under similar average path lengths, different readout modes performed differently, with different path length distributions. In general, as the shorter paths contributed relatively more in the overall distribution, the performance increased. The no-avg readout mode performed the worse, with the

path length distribution dominated by longest paths (blue distributions in Figs. 6e,f); early-avg performed better, with shorter paths contributing more to the distribution (orange distributions in the figure); late-avg and 2-avg performed the best, with even more contributions from shorter paths (green and red distributions in the figures).

With the above observations, we hypothesized that shorter paths contributed more to the model performance compared to longer ones. To verify this hypothesis, we performed ablation studies on 7-iteration models by removing paths of certain lengths from the full models that have all the paths. Consistent with our hypothesis, models with shorter paths ablated outperformed those with longer paths ablated, across readout modes (Figs. 6g,h,i as well as Appendix G); when three paths were removed, removing shorter paths (black circle in Fig. 6i) gave larger performance decrease compared to removing longer paths. There may be some interchangeability between paths of adjacent lengths, as removing a single path (Figs. 6g) had little impact on performance.

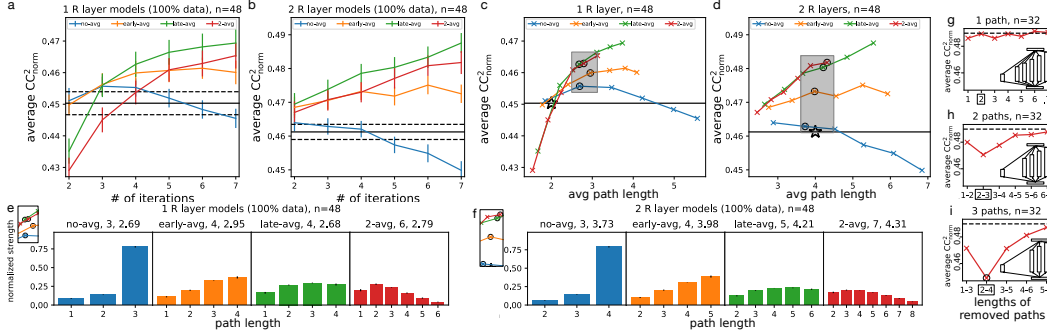


Figure 6: Path length and diversity explained performance differences across readout modes. (a),(b) are similar to Fig. 3d, except that results are aggregated over all one- and two-recurrent-layer models, respectively. (c),(d) are the same as (a),(b), with the horizontal axis showing average path lengths instead; error bars are omitted for clarity. (e),(f) show the path length distributions of example models highlighted in (c),(d), with each subtitle showing the readout mode, the number of iterations, and the average path length. (a)-(f) are based on models trained on all available training data of NS 2250; more results on models trained with other amounts of training data and the other data set can be found in Appendix F. (g)-(i) show performance metrics of ablated 2-layer, 7-iteration models with 2-avg readout mode, with 1, 2, or 3 paths removed at a time; inside each panel, the inset shows the multi-path ensemble diagram of an example ablated model indicated by the rectangle on the horizontal axis and the dashed line shows the performance of the full model with no path removed; only results for readout mode 2-avg are shown here and additional results can be found in Appendix G.

4.3.2 Recurrent models outperformed feed-forward ones of similar depths via implicit and compact multi-path ensembles

With the above explanation of performance differences among recurrent models using path length and diversity, we can now easily see why recurrent models outperformed feed-forward models matched in model size and hyperparameters (Figs. 6a,b). First, a feed-forward model can be viewed as a recurrent model with the least balanced path distribution and therefore recurrent models with non-trivial path distributions had no worse performance than feed-forward ones with similar average path lengths (Fig. 6d). Second, recurrent models with a higher number of iterations have both more diverse path distributions and deeper path lengths than matched feed-forward models; both of these allow recurrent models to approximate the complex function underlying recurrent biological circuits with more flexibility compared to feed-forward models matched in model size and hyperparameters (Fig. 6c).

5 Discussion

In this paper, we demonstrated that recurrent models consistently outperformed feed-forward ones with matched size and hyperparameters in a neural response prediction task under tens of thousands of hyperparameter settings (Section 4.1). Other recent studies in neural response prediction using

neural network models have also explored the efficacy of divisive normalization, a form of recurrent circuit, in neural prediction [34], or the use of LSTMs to predict neural response dynamics [14]. Our use of a recurrent circuit, for the first time, to predict the mean neural response is, in fact, a bit unorthodox; this, however, is necessary as it allows us to make an extensive, fair, and direct comparison of recurrent against feed-forward models with matched model sizes and hyperparameters.

The advantage of recurrent models relative to their corresponding feed-forward counterparts was considerable (up to 11 %) when the training data was limited. Performance improvement using bio-inspired deep recurrent networks has also been demonstrated earlier by others for image classification tasks [12, 13, 15], though the underlying computational reasons remain uncertain. Here, we propose that recurrent computation can be approximately conceptualized as an ensemble of feed-forward paths with shared parameters (Section 4.2). Treating recurrent computation as a multi-path ensemble is novel even though multi-path ensembles have been evoked to explain and develop deep networks with residual connections [20, 21]. We derived approximate multi-path models from recurrent networks and demonstrated the validity of the approximation empirically. We found that a balance of short and long paths in the ensemble was necessary for the recurrent model to achieve the best performance (Section 4.3); on our data sets, models with more relative weight on shorter paths tended to perform better than models with more relative weight on longer paths. We established these observations by comparing different readout modes in terms of their multi-path ensembles. In particular, we found that better performing readout modes have their path length distribution more concentrated at shorter paths and removing shorter paths had more impact on the performance than removing longer paths in an ablation study. The relative importance of shorter paths over longer ones might be data set- and task-dependent and requires further investigation.

In earlier studies of recurrent networks, typically only the responses of the last iteration in a recurrent layer were passed onto higher layers; such usage of recurrent-layer responses corresponds to no-avg readout mode in our study. We found that explicitly taking into account the response history of all iterations could increase the diversity of pathways in a recurrent model’s multi-path ensemble (Fig. 6) and increase model performance over the “vanilla” no-avg readout mode (Fig. 3). Different readout modes essentially represent different weight assignments to intermediate outputs at different iterations (Section 3.2); our exploration of different readout modes show that a balance of early and late information across iterations, or equivalently a balance of short and paths in the corresponding multi-path ensemble, is necessary for the recurrent model to achieve the best performance.

Here, we focus on the simplest recurrent models with one or two recurrent layers for the neural response prediction task [9] because they are simple enough to allow explicit path enumerations and fair, extensive comparisons against feed-forward models with matched sizes and hyperparameters. There are biologically inspired recurrent deep networks with more complicated architectures [12, 13, 15, 35] that are effective in image classification and video prediction tasks; in principle these models can also be formulated in terms of multi-path models, though their complexities make fair, extensive comparisons against feed-forward models difficult. Our study, using a simpler model and a simpler (yet still challenging) task, suggests that a key factor underlying the good performance of all recurrent models is that recurrent computation generates a compact and implicit multi-path ensemble that might approximate complex functions with greater flexibility and efficiency.

Broader Impact

Recurrent neural circuits are ubiquitous in the brain; thus elucidating the computational principles and rationales of recurrent circuits is important for understanding the brain. This study demonstrates the performance advantages of recurrent models over feed-forward models for characterizing and predicting responses of neurons in the early visual cortex. Further, it provides a novel approach for approximating recurrent models with multi-path ensembles that help us understand why recurrent models are superior in this specific neural response prediction task. Such approach could potentially be generalized to understand deeper recurrent networks in general. Thus, our work should have a broader positive impact in machine learning as well.

At this time, we cannot envision any negative consequence to arise out of this research.

Acknowledgments and Disclosure of Funding

TBD.

References

- [1] William F. Kindel, Elijah D. Christensen, and Joel Zylberberg. Using deep learning to probe the neural code for images in primary visual cortex. *Journal of Vision*, 19(4):29–29, 04 2019. ISSN 1534-7362. doi: 10.1167/19.4.29. URL <https://doi.org/10.1167/19.4.29>.
- [2] David Klindt, Alexander S. Ecker, Thomas Euler, and Matthias Bethge. Neural system identification for large populations separating "what" and "where". In Isabelle Guyon, Ulrike von Luxburg, Samy Bengio, Hanna M. Wallach, Rob Fergus, S. V. N. Vishwanathan, and Roman Garnett, editors, *Advances in Neural Information Processing Systems 30: Annual Conference on Neural Information Processing Systems 2017, 4-9 December 2017, Long Beach, CA, USA*, pages 3509–3519, 2017. URL <http://papers.nips.cc/paper/6942-neural-system-identification-for-large-populations-separating-what-and-where>.
- [3] Daniel L K Yamins and James J DiCarlo. Using goal-driven deep learning models to understand sensory cortex. *Nature Neuroscience*, 19(3):356–365, February 2016. doi: 10.1038/nn.4244. URL <http://www.nature.com/doifinder/10.1038/nn.4244>.
- [4] Yimeng Zhang, Tai Sing Lee, Ming Li, Fang Liu, and Shiming Tang. Convolutional neural network models of v1 responses to complex patterns. *Journal of Computational Neuroscience*, 46(1):33–54, Feb 2019. ISSN 1573-6873. doi: 10.1007/s10827-018-0687-7. URL <https://doi.org/10.1007/s10827-018-0687-7>.
- [5] Santiago A. Cadena, George H. Denfield, Edgar Y. Walker, Leon A. Gatys, Andreas S. Tolias, Matthias Bethge, and Alexander S. Ecker. Deep convolutional models improve predictions of macaque v1 responses to natural images. *PLOS Computational Biology*, 15(4):1–27, 04 2019. doi: 10.1371/journal.pcbi.1006897. URL <https://doi.org/10.1371/journal.pcbi.1006897>.
- [6] Nikolaus Kriegeskorte. Deep neural networks: A new framework for modeling biological vision and brain information processing. *Annual Review of Vision Science*, 1(1):417–446, 2015. doi: 10.1146/annurev-vision-082114-035447. URL <https://doi.org/10.1146/annurev-vision-082114-035447>. PMID: 28532370.
- [7] Daniel J. Felleman and David C. Van Essen. Distributed Hierarchical Processing in the Primate Cerebral Cortex. *Cerebral Cortex*, 1(1):1–47, 01 1991. ISSN 1047-3211. doi: 10.1093/cercor/1.1.1-a. URL <https://doi.org/10.1093/cercor/1.1.1-a>.
- [8] Nikola T. Markov, Julien Vezoli, Pascal Chameau, Arnaud Falchier, René Quilodran, Cyril Huisoud, Camille Lamy, Pierre Misery, Pascale Giroud, Shimon Ullman, Pascal Barone, Colette Dehay, Kenneth Knoblauch, and Henry Kennedy. Anatomy of hierarchy: Feedforward and feedback pathways in macaque visual cortex. *Journal of Comparative Neurology*, 522(1):225–259, 2014. doi: <https://doi.org/10.1002/cne.23458>. URL <https://onlinelibrary.wiley.com/doi/abs/10.1002/cne.23458>.
- [9] Courtney J. Sporer, Tim C. Kietzmann, Johannes Mehrer, Ian Charest, and Nikolaus Kriegeskorte. Recurrent neural networks can explain flexible trading of speed and accuracy in biological vision. *PLOS Computational Biology*, 16(10):1–27, 10 2020. doi: 10.1371/journal.pcbi.1008215. URL <https://doi.org/10.1371/journal.pcbi.1008215>.
- [10] Tim C. Kietzmann, Courtney J. Sporer, Lynn K. A. Sörensen, Radoslaw M. Cichy, Olaf Hauk, and Nikolaus Kriegeskorte. Recurrence is required to capture the representational dynamics of the human visual system. *Proceedings of the National Academy of Sciences*, 116(43):21854–21863, 2019. ISSN 0027-8424. doi: 10.1073/pnas.1905544116. URL <https://www.pnas.org/content/116/43/21854>.

- [11] Mitesh K. Kapadia, Gerald Westheimer, and Charles D. Gilbert. Spatial distribution of contextual interactions in primary visual cortex and in visual perception. *Journal of Neurophysiology*, 84 (4):2048–2062, 2000. doi: 10.1152/jn.2000.84.4.2048. URL <https://doi.org/10.1152/jn.2000.84.4.2048>. PMID: 11024097.
- [12] Aran Nayebi, Daniel Bear, Jonas Kubilius, Kohitij Kar, Surya Ganguli, David Sussillo, James J. DiCarlo, and Daniel L. K. Yamins. Task-driven convolutional recurrent models of the visual system. *CoRR*, abs/1807.00053, 2018. URL <http://arxiv.org/abs/1807.00053>.
- [13] Jonas Kubilius, Martin Schrimpf, Ha Hong, Najib J. Majaj, Rishi Rajalingham, Elias B. Issa, Kohitij Kar, Pouya Bashivan, Jonathan Prescott-Roy, Kailyn Schmidt, Aran Nayebi, Daniel Bear, Daniel L. Yamins, and James J. DiCarlo. Brain-like object recognition with high-performing shallow recurrent anns. In Hanna M. Wallach, Hugo Larochelle, Alina Beygelzimer, Florence d’Alché-Buc, Emily B. Fox, and Roman Garnett, editors, *Advances in Neural Information Processing Systems 32: Annual Conference on Neural Information Processing Systems 2019, NeurIPS 2019, December 8-14, 2019, Vancouver, BC, Canada*, pages 12785–12796, 2019. URL <https://proceedings.neurips.cc/paper/2019/hash/7813d1590d28a7dd372ad54b5d29d033-Abstract.html>.
- [14] Lane T McIntosh, Niru Maheswaranathan, Aran Nayebi, Surya Ganguli, and Stephen A Baccus. Deep Learning Models of the Retinal Response to Natural Scenes. *ArXiv e-prints*, q-bio.NC, February 2017. URL <https://arxiv.org/abs/1702.01825>.
- [15] Kuan Han, Haiguang Wen, Yizhen Zhang, Di Fu, Eugenio Culurciello, and Zhongming Liu. Deep predictive coding network with local recurrent processing for object recognition. In Samy Bengio, Hanna M. Wallach, Hugo Larochelle, Kristen Grauman, Nicolò Cesa-Bianchi, and Roman Garnett, editors, *Advances in Neural Information Processing Systems 31: Annual Conference on Neural Information Processing Systems 2018, NeurIPS 2018, 3-8 December 2018, Montréal, Canada.*, pages 9221–9233, 2018. URL <http://papers.nips.cc/paper/8133-deep-predictive-coding-network-with-local-recurrent-processing-for-object-recognition>.
- [16] Rupesh Kumar Srivastava, Klaus Greff, and Jürgen Schmidhuber. Highway networks. *CoRR*, abs/1505.00387, 2015. URL <http://arxiv.org/abs/1505.00387>.
- [17] Kaiming He, Xiangyu Zhang, Shaoqing Ren, and Jian Sun. Deep residual learning for image recognition. In *2016 IEEE Conference on Computer Vision and Pattern Recognition, CVPR 2016, Las Vegas, NV, USA, June 27-30, 2016*, pages 770–778. IEEE Computer Society, 2016. doi: 10.1109/CVPR.2016.90. URL <https://doi.org/10.1109/CVPR.2016.90>.
- [18] Kaiming He, Xiangyu Zhang, Shaoqing Ren, and Jian Sun. Identity mappings in deep residual networks. In Bastian Leibe, Jiri Matas, Nicu Sebe, and Max Welling, editors, *Computer Vision - ECCV 2016 - 14th European Conference, Amsterdam, The Netherlands, October 11-14, 2016, Proceedings, Part IV*, volume 9908 of *Lecture Notes in Computer Science*, pages 630–645. Springer, 2016. doi: 10.1007/978-3-319-46493-0_38. URL https://doi.org/10.1007/978-3-319-46493-0_38.
- [19] Gustav Larsson, Michael Maire, and Gregory Shakhnarovich. Fractalnet: Ultra-deep neural networks without residuals. In *5th International Conference on Learning Representations, ICLR 2017, Toulon, France, April 24-26, 2017, Conference Track Proceedings*. OpenReview.net, 2017. URL <https://openreview.net/forum?id=S1VaB4cex>.
- [20] Gao Huang, Zhuang Liu, Laurens van der Maaten, and Kilian Q. Weinberger. Densely connected convolutional networks. In *2017 IEEE Conference on Computer Vision and Pattern Recognition, CVPR 2017, Honolulu, HI, USA, July 21-26, 2017*, pages 2261–2269. IEEE Computer Society, 2017. doi: 10.1109/CVPR.2017.243. URL <https://doi.org/10.1109/CVPR.2017.243>.
- [21] Andreas Veit, Michael J Wilber, and Serge Belongie. Residual networks behave like ensembles of relatively shallow networks. In D. Lee, M. Sugiyama, U. Luxburg, I. Guyon, and R. Garnett, editors, *Advances in Neural Information Processing Systems*, volume 29, pages 550–558. Curran Associates, Inc., 2016. URL <https://proceedings.neurips.cc/paper/2016/file/37bc2f75bf1bcfe8450a1a41c200364c-Paper.pdf>.

- [22] Qianli Liao and Tomaso A. Poggio. Bridging the gaps between residual learning, recurrent neural networks and visual cortex. *CoRR*, abs/1604.03640, 2016. URL <http://arxiv.org/abs/1604.03640>.
- [23] Tian Qi Chen, Yulia Rubanova, Jesse Bettencourt, and David Duvenaud. Neural ordinary differential equations. In Samy Bengio, Hanna M. Wallach, Hugo Larochelle, Kristen Grauman, Nicolò Cesa-Bianchi, and Roman Garnett, editors, *Advances in Neural Information Processing Systems 31: Annual Conference on Neural Information Processing Systems 2018, NeurIPS 2018, December 3-8, 2018, Montréal, Canada*, pages 6572–6583, 2018. URL <https://proceedings.neurips.cc/paper/2018/hash/69386f6bb1dfed68692a24c8686939b9-Abstract.html>.
- [24] Shaojie Bai, J. Zico Kolter, and Vladlen Koltun. Deep equilibrium models. In Hanna M. Wallach, Hugo Larochelle, Alina Beygelzimer, Florence d’Alché-Buc, Emily B. Fox, and Roman Garnett, editors, *Advances in Neural Information Processing Systems 32: Annual Conference on Neural Information Processing Systems 2019, NeurIPS 2019, December 8-14, 2019, Vancouver, BC, Canada*, pages 688–699, 2019. URL <https://proceedings.neurips.cc/paper/2019/hash/01386bd6d8e091c2ab4c7c7de644d37b-Abstract.html>.
- [25] G. E. Hinton and R. R. Salakhutdinov. Reducing the dimensionality of data with neural networks. *Science*, 313(5786):504–507, 2006. ISSN 0036-8075. doi: 10.1126/science.1127647. URL <https://science.sciencemag.org/content/313/5786/504>.
- [26] Saizheng Zhang, Yuhuai Wu, Tong Che, Zhouhan Lin, Roland Memisevic, Ruslan Salakhutdinov, and Yoshua Bengio. Architectural complexity measures of recurrent neural networks. In Daniel D. Lee, Masashi Sugiyama, Ulrike von Luxburg, Isabelle Guyon, and Roman Garnett, editors, *Advances in Neural Information Processing Systems 29: Annual Conference on Neural Information Processing Systems 2016, December 5-10, 2016, Barcelona, Spain*, pages 1822–1830, 2016. URL <https://proceedings.neurips.cc/paper/2016/hash/860320be12a1c050cd7731794e231bd3-Abstract.html>.
- [27] Ruben Coen-Cagli, Adam Kohn, and Odelia Schwartz. Flexible gating of contextual influences in natural vision. *Nature Neuroscience*, 18(11):1648–1655, October 2015. doi: 10.1038/nn.4128. URL <http://www.nature.com/articles/nn.4128>.
- [28] Olga Russakovsky, Jia Deng, Hao Su, Jonathan Krause, Sanjeev Satheesh, Sean Ma, Zhiheng Huang, Andrej Karpathy, Aditya Khosla, Michael Bernstein, Alexander C. Berg, and Li Fei-Fei. ImageNet Large Scale Visual Recognition Challenge. *International Journal of Computer Vision (IJCV)*, 115(3):211–252, 2015. doi: 10.1007/s11263-015-0816-y.
- [29] Shiming Tang, Yimeng Zhang, Zhihao Li, Ming Li, Fang Liu, Hongfei Jiang, and Tai Sing Lee. Large-scale two-photon imaging revealed super-sparse population codes in the v1 superficial layer of awake monkeys. *eLife*, 7:e33370, apr 2018. ISSN 2050-084X. doi: 10.7554/eLife.33370. URL <https://doi.org/10.7554/eLife.33370>.
- [30] Sergey Ioffe and Christian Szegedy. Batch normalization: Accelerating deep network training by reducing internal covariate shift. In Francis R. Bach and David M. Blei, editors, *Proceedings of the 32nd International Conference on Machine Learning, ICML 2015, Lille, France, 6-11 July 2015*, volume 37 of *JMLR Workshop and Conference Proceedings*, pages 448–456. JMLR.org, 2015. URL <http://jmlr.org/proceedings/papers/v37/ioffe15.html>.
- [31] Adam Paszke, Sam Gross, Francisco Massa, Adam Lerer, James Bradbury, Gregory Chanan, Trevor Killeen, Zeming Lin, Natalia Gimelshein, Luca Antiga, Alban Desmaison, Andreas Köpf, Edward Yang, Zach DeVito, Martin Raison, Alykhan Tejani, Sasank Chilamkurthy, Benoit Steiner, Lu Fang, Junjie Bai, and Soumith Chintala. PyTorch: An Imperative Style, High-Performance Deep Learning Library. *arXiv e-prints*, art. arXiv:1912.01703, December 2019.
- [32] Oliver Schoppe, Nicol S. Harper, Ben D. B. Willmore, Andrew J. King, and Jan W. H. Schnupp. Measuring the performance of neural models. *Frontiers in Computational Neuroscience*, 10:10, 2016. ISSN 1662-5188. doi: 10.3389/fncom.2016.00010. URL <https://www.frontiersin.org/article/10.3389/fncom.2016.00010>.

- [33] Anne Hsu, Alexander Borst, and Frédéric Theunissen. Quantifying variability in neural responses and its application for the validation of model predictions. *Network: Computation in Neural Systems*, 15(2):91–109, May 2004. doi: 10.1088/0954-898X/15/2/002. URL <http://www.informaworld.com/openurl?genre=article&doi=10.1088/0954-898X/15/2/002&magic=crossref||D404A21C5BB053405B1A640AFFD44AE3>.
- [34] Max F. Burg, Santiago A. Cadena, George H. Denfield, Edgar Y. Walker, Andreas S. Tolias, Matthias Bethge, and Alexander S. Ecker. Learning divisive normalization in primary visual cortex. *bioRxiv*, 2020. doi: 10.1101/767285. URL <https://www.biorxiv.org/content/early/2020/07/24/767285>.
- [35] William Lotter, Gabriel Kreiman, and David Cox. Deep Predictive Coding Networks for Video Prediction and Unsupervised Learning. *arXiv e-prints*, art. arXiv:1605.08104, May 2016.

Checklist

1. For all authors...
 - (a) Do the main claims made in the abstract and introduction accurately reflect the paper’s contributions and scope? [\[Yes\]](#)
 - (b) Did you describe the limitations of your work? [\[Yes\]](#) See Section 5.
 - (c) Did you discuss any potential negative societal impacts of your work? [\[N/A\]](#) At this time, we cannot envision any negative societal consequence to arise out of this research.
 - (d) Have you read the ethics review guidelines and ensured that your paper conforms to them? [\[Yes\]](#)
2. If you are including theoretical results...
 - (a) Did you state the full set of assumptions of all theoretical results? [\[N/A\]](#)
 - (b) Did you include complete proofs of all theoretical results? [\[N/A\]](#)
3. If you ran experiments...
 - (a) Did you include the code, data, and instructions needed to reproduce the main experimental results (either in the supplemental material or as a URL)? [\[Yes\]](#) Once the paper is accepted (in order for us to remain anonymous for the review process).
 - (b) Did you specify all the training details (e.g., data splits, hyperparameters, how they were chosen)? [\[Yes\]](#) See Section 3.3 as well as Appendix C.
 - (c) Did you report error bars (e.g., with respect to the random seed after running experiments multiple times)? [\[Yes\]](#)
 - (d) Did you include the total amount of compute and the type of resources used (e.g., type of GPUs, internal cluster, or cloud provider)? [\[Yes\]](#) See Section 3.3.
4. If you are using existing assets (e.g., code, data, models) or curating/releasing new assets...
 - (a) If your work uses existing assets, did you cite the creators? [\[Yes\]](#) Tang et al. [29].
 - (b) Did you mention the license of the assets? [\[Yes\]](#) Section 3.
 - (c) Did you include any new assets either in the supplemental material or as a URL? [\[Yes\]](#) Once the paper is accepted (in order for us to remain anonymous for the review process).
 - (d) Did you discuss whether and how consent was obtained from people whose data you’re using/curating? [\[Yes\]](#) We followed the terms of the license (CC BY 4.0) attached to the data.
 - (e) Did you discuss whether the data you are using/curating contains personally identifiable information or offensive content? [\[N/A\]](#)
5. If you used crowdsourcing or conducted research with human subjects...
 - (a) Did you include the full text of instructions given to participants and screenshots, if applicable? [\[N/A\]](#)
 - (b) Did you describe any potential participant risks, with links to Institutional Review Board (IRB) approvals, if applicable? [\[N/A\]](#)
 - (c) Did you include the estimated hourly wage paid to participants and the total amount spent on participant compensation? [\[N/A\]](#)

A Details of neural data sets

Data from two series of experiments performed on an awake behaving macaque monkey acquired in our laboratory were used in this study. In both experiments, the monkey performed a fixation task. Spiking neuronal activity was acquired from V1 and V2 using an SC96 array, a 96-electrode multi-electrode array (Gray Matter Research, MT).

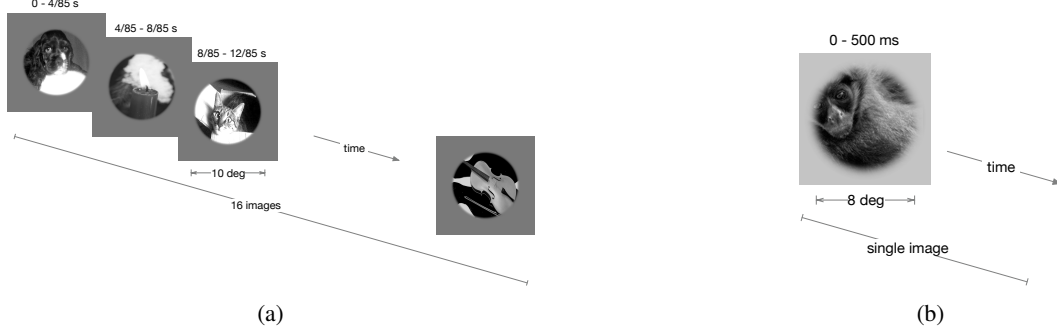


Figure 7: Stimulus presentation paradigms of a single trial, for ImageNet 8K (a) and NS 2250 (b). The style of the figure is adapted from Cadena et al. [5].

In the ImageNet 8K experiment, 8000 stimuli were presented with 16 stimuli per trial while the monkey fixated. Each trial lasted for 753 ms, and thus each image was presented for 47 ms (4 frames at 85 Hz). In the NS2250 experiment, a total of 2250 stimuli were tested. Each image was presented for 500 ms, and repeated 8 to 10 times randomly interleaved with other stimuli. Each day, 500 images were tested in 4000 trials. Five consecutive days of recording were performed. Each day 25 calibration images were also tested to allow tracking of neurons across days based on their stimulus response fingerprints. The stimulus presentation paradigms are shown in Figure 7.

For the ImageNet 8K data set, stimuli were presented in a 10° diameter circular aperture within a gray surround. The central 200 px by 200 px part used for modeling has an average RMS contrast of 0.3. For the NS 2250 data set Tang et al. [29], each image was presented within a 8° aperture. The central 148 px by 200 148 part used for modeling has an average RMS contrast of 0.27. The receptive field of the V1 and V2 neurons were typically in the range of 1-2 degree visual angle and 2-4 degree visual angle respectively.

B Details of the explored models

B.1 Baseline models

During inference, a baseline model takes an image $\mathbf{x} \in \mathbb{R}^{H \times W}$ of height H and width W as input and generates an prediction $\vec{\mathbf{r}} \in \mathbb{R}^N$ of the neural responses $\vec{\mathbf{r}} \in \mathbb{R}^N$ to the image. Mathematically, the model inference process is defined by Eqs. (1).

$$\vec{\mathbf{r}} = \text{Act}(\text{FC}(\text{Pool}(\mathbf{y}^{(M)}))) \quad (1a)$$

$$\mathbf{y}^{(m)} = \text{CPB}^{(m)}(\mathbf{y}^{(m-1)}) \quad m = 2, \dots, M \quad (1b)$$

$$\mathbf{y}^{(1)} = \text{CPB}^{(1)}(\text{BatchNorm}(\mathbf{x})) \quad (1c)$$

$$\text{CPB}^{(m)}(\mathbf{y}) = \text{Act}(\text{BatchNorm}^{(m)}(\text{Conv}^{(m)}(\mathbf{y}))) \quad (1d)$$

For a model of M convolutional processing blocks (CPBs), the model inference starts with Eq. (1c) to normalize the input image and obtain the initial CPB's output $\mathbf{y}^{(1)}$, followed by a few applications of Eq. (1b) to get outputs of later CPBs $\mathbf{y}^{(2)}, \dots, \mathbf{y}^{(M)}$. Finally, Eq. (1a) is applied to obtain the predicted neural responses $\vec{\mathbf{r}}$. Conv, BatchNorm, Act, Pool, FC represent convolution, batch normalization, nonlinear activation, average pooling, and factorized fully connected layers [2], respectively. Different

convolutional processing blocks have different hyper parameters and learned parameters, as denoted by superscripts (m) in Eq. (1d).

B.2 Recurrent models

The model inference process is defined by Eqs. (2). and the detailed information flow for a recurrent model across iterations are illustrated in Figure 8.

$$\vec{r}_{\text{no-avg}} = \text{Act}(\text{FC}(\text{Pool}(\mathbf{y}^{(M,T)}))) \quad (2a)$$

$$\vec{r}_{\text{early-avg}} = \text{Act}(\text{FC}(\text{Pool}(\bar{\mathbf{y}}^{(M,T)}))) \quad (2b)$$

$$\vec{r}_{\text{late-avg}} = \frac{1}{T} \sum_{t=1}^T \text{Act}(\text{FC}(\text{Pool}(\mathbf{y}^{(M,t)}))) \quad (2c)$$

$$\vec{r}_{2\text{-avg}} = \frac{1}{T} \sum_{t=1}^T \text{Act}(\text{FC}(\text{Pool}(\bar{\mathbf{y}}^{(M,t)}))) \quad (2d)$$

$$\bar{\mathbf{y}}^{(M,t)} = \frac{1}{t} \sum_{t'=1}^t \mathbf{y}^{(M,t')} \quad (2e)$$

$$\mathbf{y}^{(m,t)} = \text{RCPB}^{(m,t)}(\mathbf{y}^{(m-1,t)}, \mathbf{y}^{(m,t-1)}) \quad m = 2, \dots, M; t = 1, \dots, T \quad (2f)$$

$$\mathbf{y}^{(1,t)} = \text{RCPB}^{(1,t)}(\text{BatchNorm}(\mathbf{x}), \mathbf{y}^{(1,t-1)}) \quad t = 1, \dots, T \quad (2g)$$

$$\mathbf{y}^{(m,0)} = \mathbf{0} \quad (2h)$$

$$\text{RCPB}^{(m,t)}(\mathbf{y}, \mathbf{y}') = \text{Act}(\text{BatchNorm}^{(m,t)}(\text{Conv}_{\text{feed-forward}}^{(m)}(\mathbf{y}) + \text{Conv}_{\text{lateral}}^{(m)}(\mathbf{y}')))) \quad (2i)$$

For a model of M recurrent convolutional blocks (CPBs) and T iterations in total, the model inference starts with T cycles of Eqs. (2g),(2f) to obtain the responses of all M RCPBs across T iterations $\mathbf{y}^{(m,t)}$, $m = 1 \dots M$, $t = 1 \dots T$. Finally, one of Eqs. (2a),(2b),(2c),(2d) is used to obtain the final model output depending on the readout mode used (Section 3.2). The readout modes are named based on how they average the intermediate outputs across iterations (Figure 2).

1. no-avg (Figure 2a) No averaging. The intermediate output at the last iteration is passed through the remaining layers of the model to get the final output.
2. early-avg (Figure 2b) Early averaging only. It's similar to no-avg except that the average of intermediate outputs across iterations is passed through the remaining layers of the model.
3. late-avg (Figure 2c) Late averaging only. The neural response predictions based on the individual intermediate outputs across iterations are averaged as the final output.
4. 2-avg (Figure 2d) Both early and late averaging. First the cumulative averages of intermediate outputs across iterations are computed and then the neural response predictions based on these cumulative averages are further averaged as the final output.

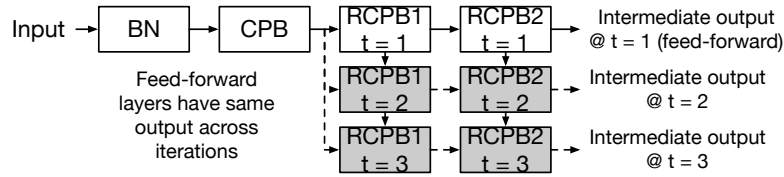


Figure 8: Information flow in the convolutional phase for a recurrent model. The example model has one CPB, two RCPBs, and three iterations in total. In the first iteration $t = 1$, the information flow is the same as that in a baseline feed-forward model. In later iterations, the output of a RCPB depends on both bottom-up and lateral inputs. The extra information flow of a recurrent model relative to a feed-forward one is shown in shaded blocks and dashed lines.

There are two details worth noting about our implementation of the recurrent model. First, RCPBs are technically not fully recurrent. As indicated by the notations in Eq. (2i), for a given RCPB, the convolution layers are fixed across iterations but different batch normalization layers are used for different iterations t . We use different batch normalization layers to accommodate different mean and variance statistics of responses across different iterations, with minimal increase in model size ($\leq 1\%$). Second, a RCPB might have fewer iterations T' than the overall model iteration T . For example, a CPB is a RCPB with $T' = 1$ iteration; there is no lateral convolutional layer or additional batch normalization layer to define model output $\mathbf{y}^{(t)}$, $t > 1$. In such cases, we use the output at iteration T' as the output for later iterations, or $\mathbf{y}^{(t)} = \mathbf{y}^{(T')}$, $t = T' + 1, \dots, T$; with such definition, Eq. (2) are applicable to recurrent models explored in this study, where each recurrent model has one CPB followed by a number of RCPBs.

C Implementation details

C.1 Data preprocessing

Following practices in the literature [2, 5], for each data set, we used cropped and downsampled images as the input and normalized average neural responses as the output for modeling purposes.

C.2 Model configurations

To comprehensively evaluate recurrent models vs. feed-forward models, we trained and tested multiple variants of recurrent and feed-forward models with different model configurations.

Kernel sizes Following previous studies [2, 5] and as well as based on our pilot experiments, in either of a feed-forward model or a recurrent model, the first convolutional layer has a relatively large kernel size (9) and subsequent layers have a small kernel size of 3. The pooling layer always has a kernel size of 3 and a stride of 3.

Feed-forward models For each data set, we trained a large set of feed-forward models with different configurations differing on aspects like amount of training data, model size, loss functions, randomness parameters, etc., as listed in Table 2. Each aspect of configuration was explored for certain reasons as follows.

- **Training data and model size-related model hyperparameters.** we explored model configurations in these two aspects because we feel training data amount and model size affect the relative performance difference between feed-forward and recurrent models. In particular, we hypothesized that the additional circuit priors from recurrent models would be more useful when there was less training data and the model size was larger.
- **Model size-independent model hyperparameters and loss functions** We explored model configurations in this aspect because we wanted to know if the advantage of recurrent models over feed-forward models is limited to certain choices of model size-independent model hyperparameters and loss functions, or if such advantage is universal across choices of model size-independent hyperparameters and loss functions.
- **Randomness hyperparameters** We explored different model initialization seeds because we wanted to obtain robust metric numbers for our models by averaging results over different seeds. Ideally we should also explore over other randomness hyperparameters, such as the seed used to split data into training, validation, and testing sets. We did not do so due to computational resource constraints.

Recurrent models For each feed-forward model, we trained 24 corresponding recurrent models of the same size, to comprehensively compare feed-forward and recurrent models. To keep the comparison as fair as possible, each of the 24 recurrent models have the same hyperparameters as the feed-forward one on those hyperparameters listed in Table 2, except with a decreased number of convolutional layers to match the model size because a recurrent convolutional processing block has roughly twice as many parameters as a convolutional processing block with the same number of channels. In particular, we replace every two CPBs of kernel size 3 in a feed-forward model with one

Table 2: Model configurations explored for feed-forward models. k denotes the kernel size for a convolutional block

Aspect	name	values explored
training data	amount of training data	25%, 50%, 100%
		(1280, 2560, 5120 for ImageNet 8K, 350, 700, 1400 for NS 2250)
model size-related model hyperparameters	# of convolutional blocks	3 (1 CPB @ $k=9$ + 2 CPBs @ $k=3$), 5 (1 CPB @ $k=9$ + 4 CPBs @ $k=3$)
	# of channels per convolutional layer	8, 16, 32, 48, 64 for ImageNet 8K, 8, 16, 32 for NS 2250
model size-independent model hyperparameters and loss functions	loss function	mean squared error, mean Poisson loss
	activation layer	ReLU, softplus
	order of BN and activation in the first convolutional block	BN before act, BN after act
randomness hyperparameters	model initialization seed	0, 1

RCPB of kernel size 3 in a recurrent model. Note that a recurrent model does not involve recurrent computation in its first CPB, which has a large kernel size of 9, and only has recurrent computation at subsequent CPBs of kernel size 3; we made this decision based our pilot experiments and for simplicity in matching the model size between recurrent and feed-forward models. In addition, the 24 recurrent models differ in their recurrence-related model hyperparameters listed as follows.

- **Number of iterations**, with six possible values 2 to 7. This hyperparameter affects the amount of recurrent computation during model training and inference. We wanted to explore this hyperparameter because obviously amount of recurrence may affect model performance. Note that we always use the same number of iterations during training and testing; e.g. a recurrent model with T iterations during training is always evaluated with T iterations during testing.
- **Readout mode**, with four possible values (no-avg, early-avg, late-avg, 2-avg; Section 3.2). We want to explore this hyperparameter because we wanted to know if some readout modes perform better than others and if there exists some optimal way to make use of intermediate outputs generated by a recurrent model.

C.3 Model optimization

We trained all models using PyTorch [31] and followed Klindt et al. [2] for model optimization.

Objective function For each model, the objective function to be minimized was the sum of two parts.

Neural prediction loss Depending on the choice of hyperparameters (Section 3.3), the loss can be either mean squared loss or mean Poisson loss between the predicted neural response and recorded ground truth averaged across neurons and images. Note that for recurrent models with late-avg or 2-avg readout modes, following the practice in Spoerer et al. [9], we computed the neural prediction loss by averaging the losses over individual iterations.

Regularization terms We applied L1 sparsity penalties as regularization; in addition, for the first convolutional layer of the model, we applied smoothness regularization as in Section 5.2 of Klindt et al. [2].

Optimization algorithm Given the objective function, we used the same optimization algorithm as in the public code of Klindt et al. [2]; in particular model parameters were optimized sequentially

in three phases, by three Adam optimizers with decreasing learning rates. Early stopping was applied in each phase, guided by the neural prediction loss evaluated on the validation set. For each data set, roughly 64 %, 16 %, and 20 % of images were used for training, validation, and testing, respectively. Due to computation resource constraints, we only created one particular split of training, validation, and testing sets for each of ImageNet 8K and NS 2250. To make sure our conclusions were not dependent on particular data splits, we retrained a subset of models using another data split and found similar results (Appendix H).

C.4 Model performance evaluation in detail

Given a trained model, we use average CC_{norm}^2 over all neurons to quantify its performance on a data set. For each neuron, we compute its CC_{norm}^2 based on Eqs. (3).

$$CC_{\text{norm}}^2 = \frac{CC_{\text{raw}}^2}{CC_{\text{max}}^2} \quad (3a)$$

$$CC_{\text{raw}} = \text{Pearson}(\vec{r}, \hat{\vec{r}}) \quad (3b)$$

$$CC_{\text{max}} = \sqrt{\frac{\text{Var}(\{\sum_k r_{m,k}\}) - \sum_k \text{Var}(\{r_{m,k}\})}{K(K-1)\text{Var}(\{r_m\})}}. \quad (3c)$$

$$\vec{r} = (r_1, r_2, \dots, r_M) \quad (3d)$$

$$r_m = \frac{\sum_{k=1}^K r_{m,k}}{K} \quad (3e)$$

Concretely, we first compute the raw Pearson correlation CC_{raw} between the ground truth trial-averaged neural responses \vec{r} as defined by Eqs. (3d),(3e) and the model responses $\hat{\vec{r}}$ using Eq. (3b). We then divide CC_{raw} by CC_{max} , which is defined in Eq. (3c) and estimates the maximal Pearson correlation coefficient an ideal model can achieve given the noise in the neural data [32, 33]; inside the square root of Eq. (3c), the numerator is the difference between variance of response sums per stimulus $\sum_k r_{m,k}$ and sum of response variances per trial $\text{Var}(\{r_{m,k}\})$, and the denominator is the variance of the trial-average neural responses scaled by a factor related to the number of trials K . Finally, we get the square of the normalized Pearson correlation coefficient using Eq. (3a). As squared CC_{raw} gives the fraction of variance in neural responses explained by the model in a simple linear regression, squared CC_{norm} gives the normalized explained variance that accounts for noise in the neural data. Note that we used neural responses on all stimuli instead of on testing set stimuli to compute CC_{max} in Eq. (3c) for more accurate estimation. In addition, because the NS2250 data set has a variable number of trials per image (8 to 10), we only used the first eight trials for simplicity.

While the derivation of CC_{max} is technically complicated, it's positively related with the Pearson correlation between mean responses computed over half of trials and those computed over the other half [32, 33]. We use CC_{norm}^2 instead of raw CC_{raw}^2 to quantify model performance because the former is more robust to trial to trial response fluctuations. Our main results in Section 4.1 still hold if we measure the performance in CC_{raw}^2 . Note that the trial-to-trial neural response data from the ImageNet 8K data were less stable compared to those from the NS 2250 data, resulting in a lower CC_{max} for ImageNet 8K. In turn, due to the normalization effects of CC_{max}^2 on the raw squared Pearson correlation CC_{raw}^2 , the model performance metrics to be presented in Section 4 were generally higher on ImageNet 8K than NS 2250, although the performance metrics on ImageNet 8K were lower than NS 2250 if measured in CC_{raw}^2 .

D Additional results on the comparison of recurrent and feed-forward models

D.1 Additional results on NS 2250

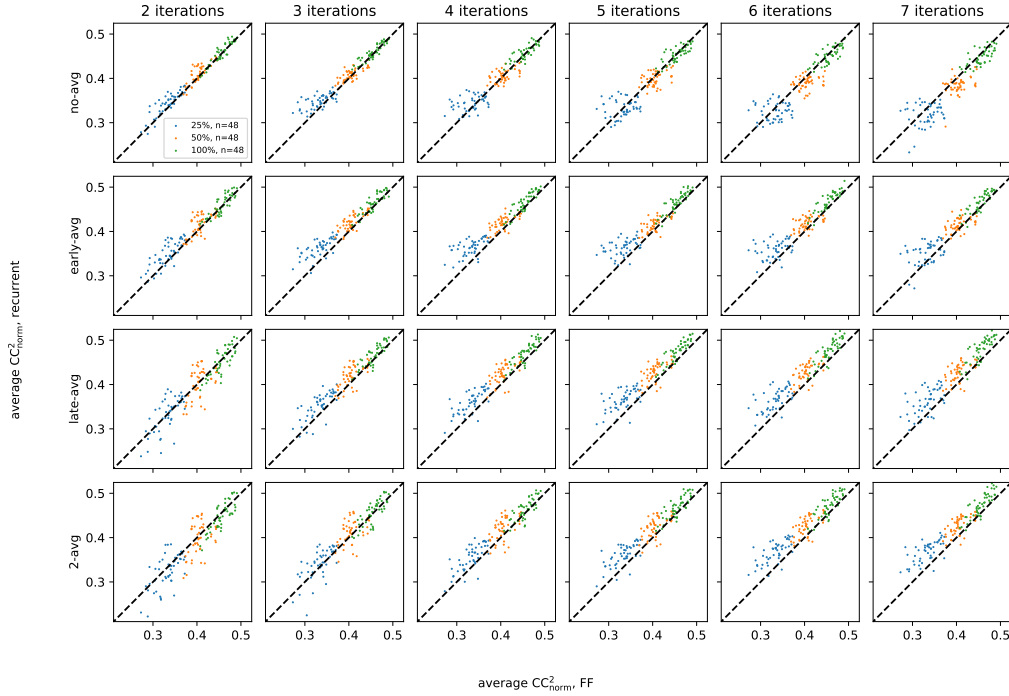


Figure 9: Figure 3a, zoomed in, showing recurrent models vs. similarly-sized feed-forward models under 24 combinations of readout mode and number of iterations, for NS 2250 data. Panels in the same row have the same readout mode as indicated on the left of the whole figure, and panels in the same column have the same number of iterations as indicated on the top of the whole figure. While we trained 96 feed-forward models and their corresponding recurrent models under 24 conditions (Section 3.3) for each explored training data size, each panel only shows $n = 48$ pairs of (aggregated) recurrent vs. feed-forward models per training data size, as we averaged the results over the two explored model parameter initialization seeds for more robust metrics (Section 3.3). In each panel, model pairs trained under different amounts of training data (25%, 50%, 100%) are shown in different colors, with 48 (aggregated) model pairs for each explored training data size.

D.2 Additional results on ImageNet 8K

Table 3: Recurrent models vs. feed-forward models on the ImageNet 8K data set, presented in the same style as Table 1.

training data	FF avg perf	best readout mode, # of iter for R	performance gain (%)
25% (1280)	0.4872	2-avg, 7	6.5039
50% (2560)	0.5896	late-avg, 6	3.5247
100% (5120)	0.6434	late-avg, 7	2.2090

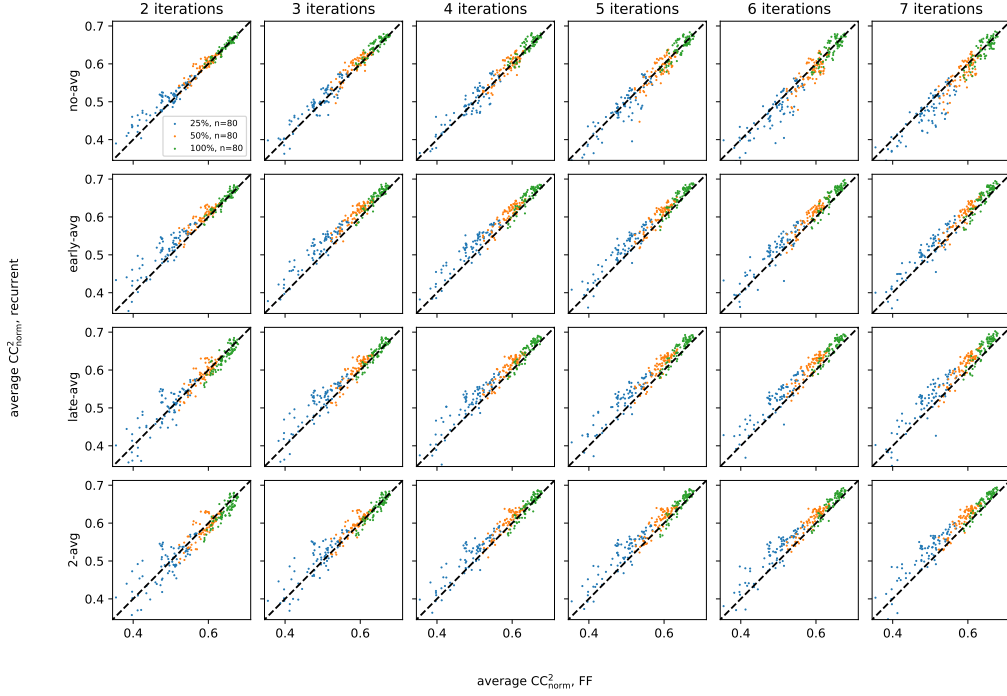


Figure 10: ImageNet 8K version of Figure 9.

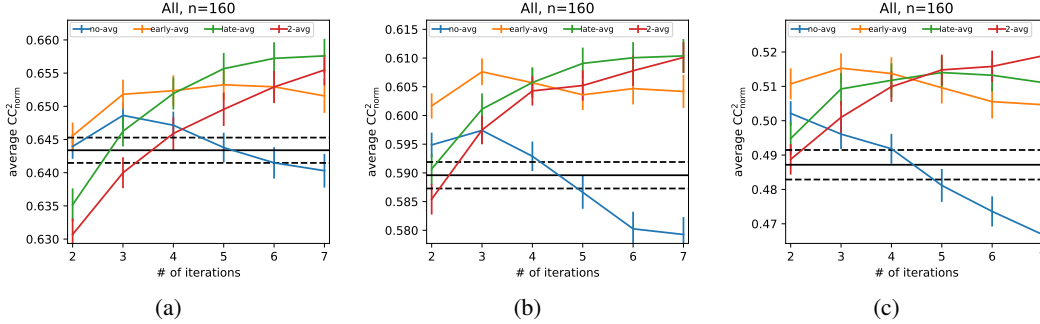


Figure 11: Recurrent models vs. feed-forward models on the ImageNet 8K data. (a), (b), (c) correspond to Figures 3d,e,f for the NS 2250, respectively.

E Multi-path models as approximations of recurrent models

In Section 4.2, to demonstrate the validity of multi-path reformulation, we converted each recurrent model into a corresponding multi-path model following the procedure illustrated in Figure 4 and then retrained the multi-path model from scratch under the same hyperparameters as the original recurrent model. Unlike the recurrent model which combines multiple information flow paths using shared components (Figure 4a), the multi-path model has separate feed-forward paths (Figure 4n) with shared convolutional weights. Full results on the comparison of multi-path vs. recurrent models are shown in Figures 12, 13 in addition to those in Figures 4c,d. Note that the total number of multi-path models (sum of all n 's in the figure) was lower than the total number of recurrent models we had, because larger models, like those with three layers and more than 32 channels, did not fit in GPU memory and so could not be trained.

In addition, note that the retrained multi-path models have shared parameters across paths for convolutional layers but separate parameters for batch normalization layers. While sharing batch normalization layers results in a more faithful reformulation of the original recurrent model, in

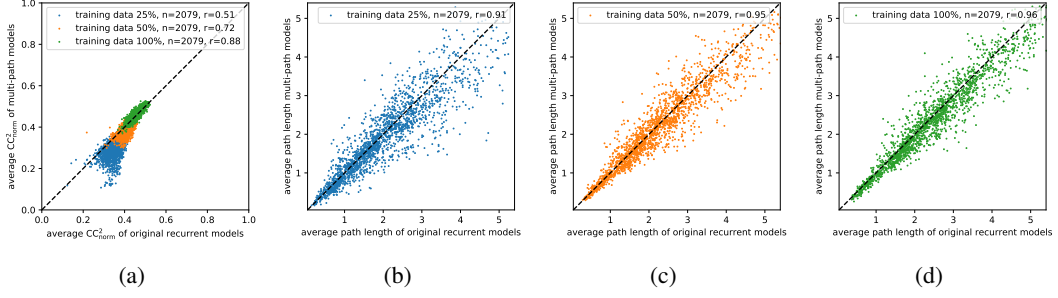


Figure 12: Retrained multi-path models vs. original recurrent models. **(a)** contains all the information in Figure 4c as well as results for models trained on 25 % and 50 % of training data; **(d)** is the same as Figure 4d; **(b),(c)** are similar to **(d)** but show results for models trained on 25 % and 50 % of training data, respectively.

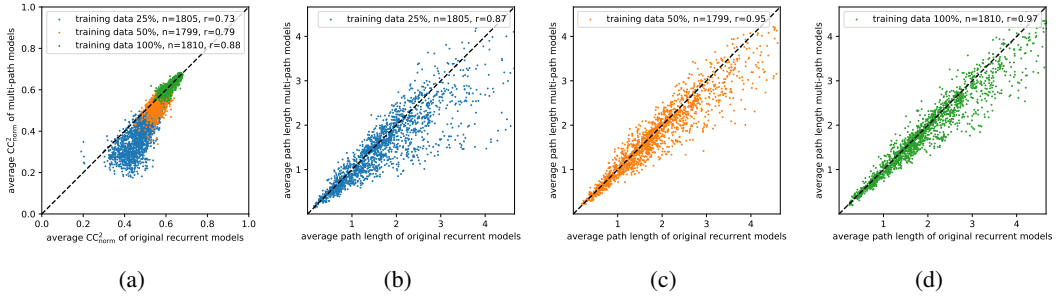


Figure 13: The ImageNet 8K version of Figure 12.

practice we found that separate BN parameters gave much better performance at a cost of small model size increase and sharing BN parameters made multi-path models perform much worse, since each BN layer has to learn the statistics over multiple paths in this setting.

F Understanding differences among models via path length and diversity

F.1 NS 2250

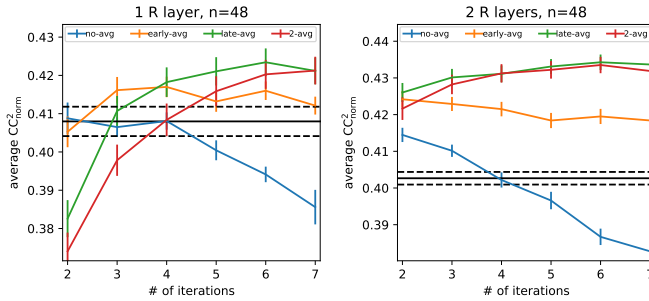


Figure 14: Same as Figures 6a,b, with 50 % of available training data.

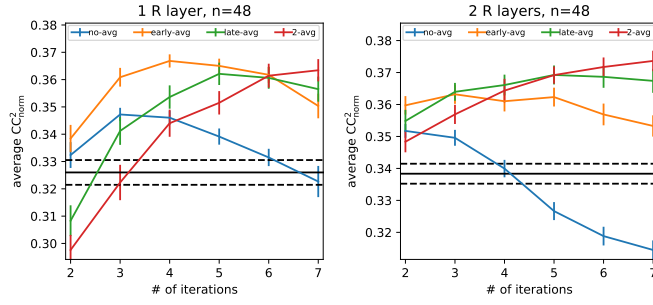


Figure 15: Same as Figures 6a,b, with 25 % of available training data.

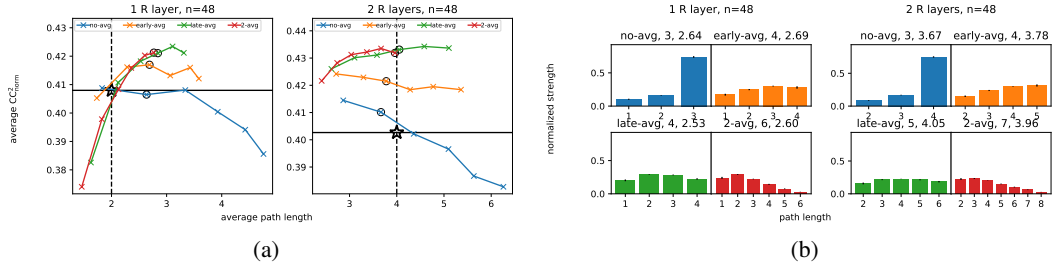


Figure 16: Figures 6c-f for models trained on 50 % of data.

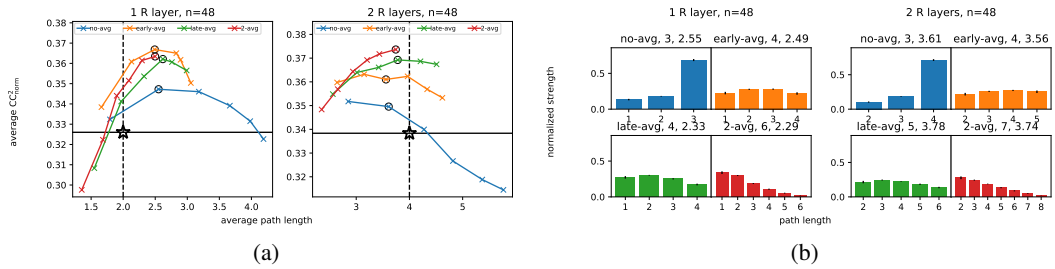


Figure 17: Figures 6c-f for models trained on 25 % of data.

F.2 ImageNet 8K

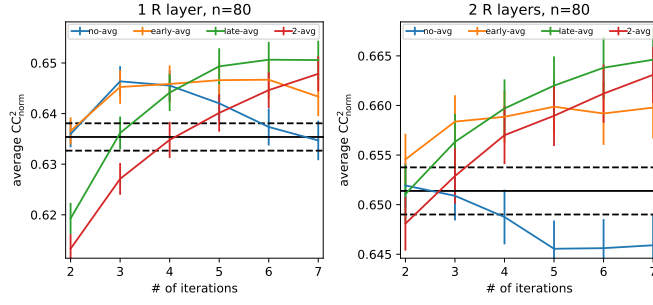


Figure 18: ImageNet 8K version of Figures 6a,b.

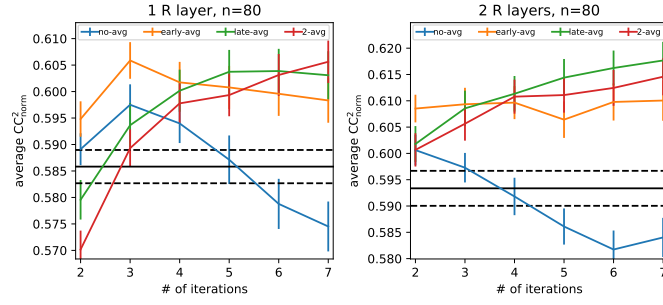


Figure 19: ImageNet 8K version of Figure 14.

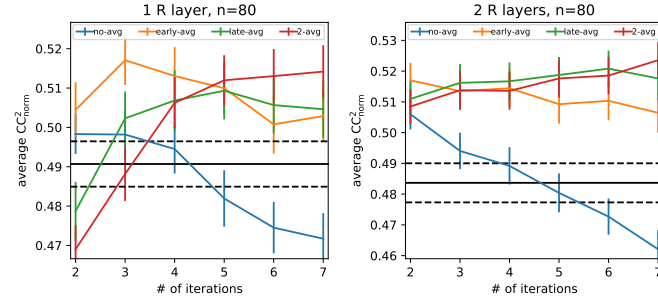


Figure 20: ImageNet 8K version of Figure 15.

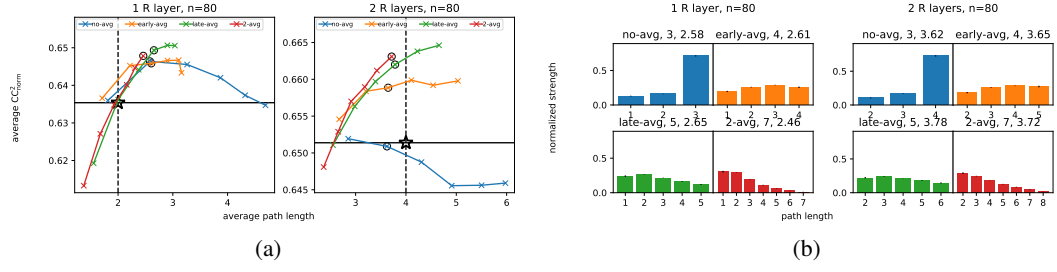


Figure 21: ImageNet 8K version of Figures 6c-f.

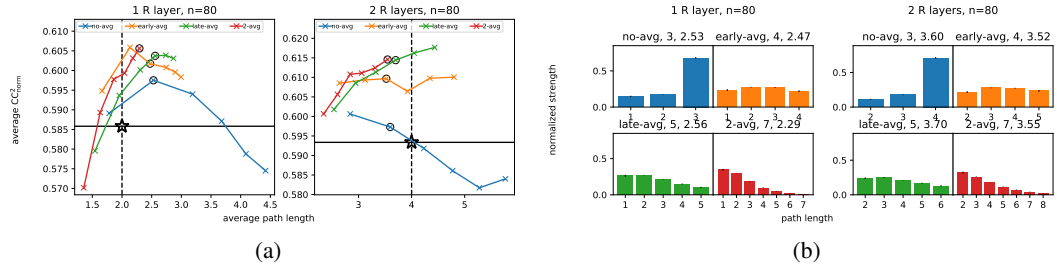


Figure 22: ImageNet 8K version of Figure 16.

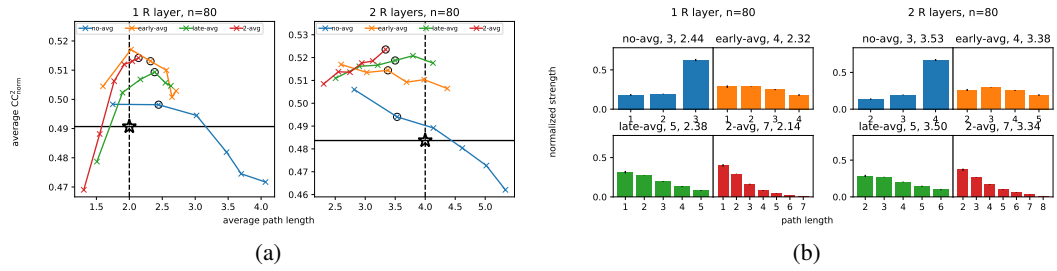


Figure 23: ImageNet 8K version of Figure 17.

G Ablation study

To compute the baseline shown as horizontal dashed lines in Figures 6g-i, 25, and 24, we trained the multi-path models corresponding to the original recurrent models with 2 layers, 7 iterations, and 16 or 32 channels using 100% of training data. The construction of multi-path models and their subtle differences from the original recurrent models are described in Appendix E. We used all the training data because the reformulation of recurrent models as multi-path models worked better with more training data (Figures 12,13); we did not train recurrent models with other numbers of layers or channels because models with 3 layers or more than 32 channels exceeded GPU memory limits during training and 8-channel recurrent models did not outperform feed-forward models much. In addition, for the ImageNet 8K data, eight multi-path models exceeded GPU memory limits during training, causing n , the number of models per data point to be 24 in Figure 24 instead of 32 as in Figure 25.

To compute the performance metrics of ablated models in the figures, we trained additional multi-path models like those for getting the baseline, but with paths of certain lengths removed. In each of the figures, the left panel shows the performance metric change when paths of a particular length (1,2,3,4,5,6) were removed; the middle panel shows the performance metrics change when paths of two adjacent lengths (1-2, 2-3, 3-4, 4-5, 5-6) were removed; the right panel shows the performance metric change when paths of three adjacent lengths (1-3, 2-4, 3-5, 4-6, 5-7) were removed.

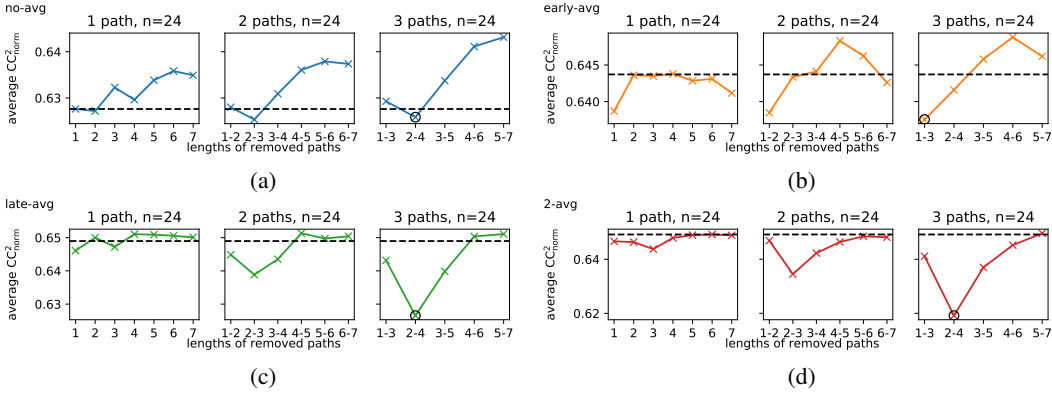


Figure 24: Performance metrics of ablated 2-layer, 7-iteration models of 16 and 32 channels on ImageNet 8K data, with 1, 2, or 3 paths removed at a time. Different panels (a) through (d) show results under different readout modes as denoted on the top left corner of each panel, and each panels shows results of models with 1, 2, 3 paths removed from left to right. Dotted lines show the performance metrics of full models that have all paths. Each circle denotes the worst performing ablation configuration with 3 paths removed. For each readout mode, on top of each of the four sub panels, the n in the title denotes the number of underlying models used to compute each data point. All models shown here were trained using all the available training data as the multi-path ensemble framework worked better with more data (Section 4.2). Models with 3-layers or more channels were not studied due to GPU memory limits as explained in Appendix G.

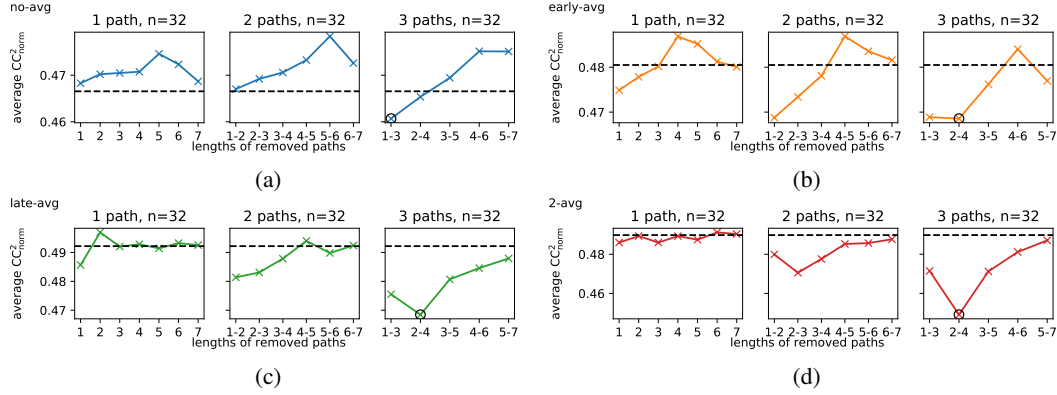


Figure 25: NS 2250 version of Figure 24.

H Additional results using a different random seed for splitting 8K data into training, validation, and testing sets

Due to resource limits, for each data set, we’ve presented all the results in this study using a single random seed for splitting data into training, validation, and testing sets (Section 3.3). As a sanity check, we trained additional models with a different random seed for data splitting, in order to make sure that our main results that recurrent models outperformed feed-forward ones would still hold regardless of data splitting. Due to resource limits we only retrained the subset of models using 100% of training data on ImageNet 8K; results on these retrained models were consistent with the results on the original models as shown below in Figure 26.

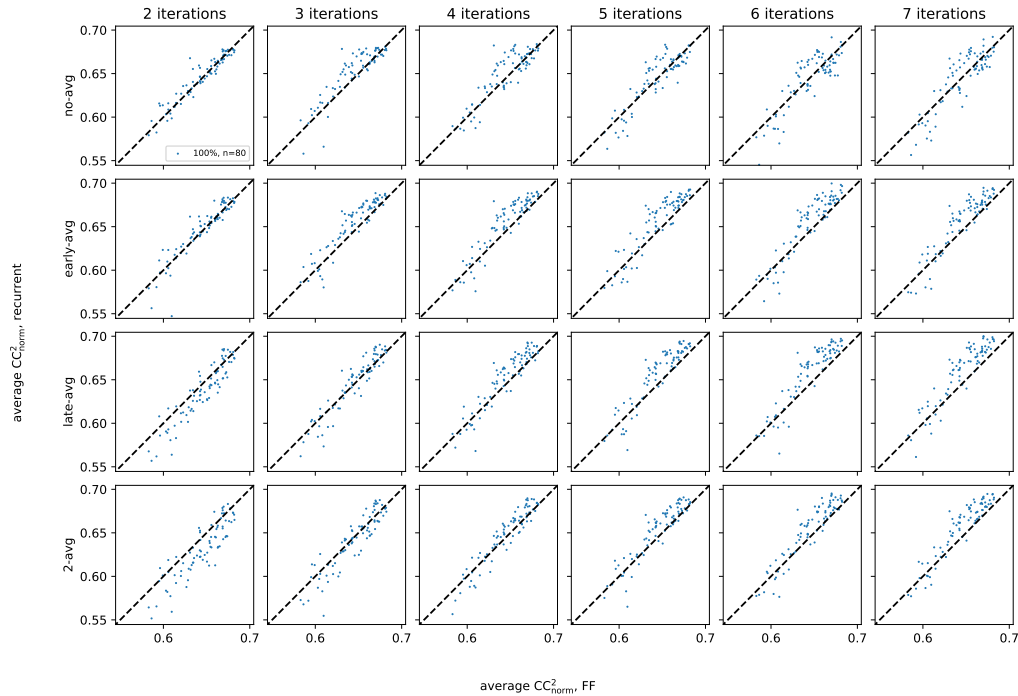


Figure 26: Same as Figure 10, using another data splitting seed and only using 100% of training data.

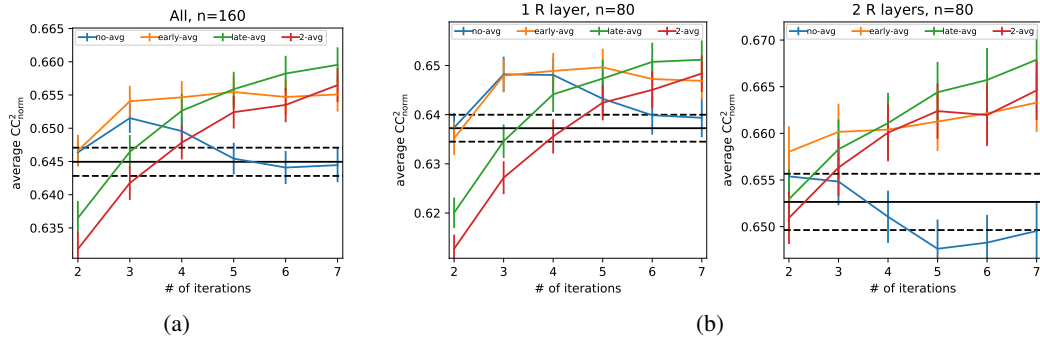


Figure 27: Same as Figure 18, using another data splitting seed.